



Article

# Mechanism Exploration of Amyloid- $\beta$ -42 Disaggregation by Single-Chain Variable Fragments of Alzheimer's Disease Therapeutic Antibodies

Xing Fan <sup>1,†</sup>, Lipeng Xu <sup>1,†</sup> , Jianhao Zhang <sup>1</sup>, Yidan Wang <sup>1</sup>, Zirui Wu <sup>1</sup>, Wenjing Sun <sup>1</sup>, Xin Yao <sup>1</sup>, Xu Wang <sup>1</sup>, Shanshan Guan <sup>2,\*</sup> and Yaming Shan <sup>1,3,\*</sup>

<sup>1</sup> National Engineering Laboratory for AIDS Vaccine, School of Life Sciences, Jilin University, Changchun 130012, China; fanxing9919@mails.jlu.edu.cn (X.F.); xulp22@mails.jlu.edu.cn (L.X.); zhangjh1319@mails.jlu.edu.cn (J.Z.); wuzr2021@jlu.edu.cn (Z.W.); sunwj1319@mails.jlu.edu.cn (W.S.); yaoxin21@mails.jlu.edu.cn (X.Y.); wangx22@mails.jlu.edu.cn (X.W.)

<sup>2</sup> College of Biology and Food Engineering, Jilin Engineering Normal University, Changchun 130052, China

<sup>3</sup> Key Laboratory for Molecular Enzymology and Engineering, The Ministry of Education, School of Life Sciences, Jilin University, Changchun 130012, China

\* Correspondence: guanshanshan@jlenu.edu.cn (S.G.); shanyam@jlu.edu.cn (Y.S.); Tel.: +86-431-89228979 (Y.S.)

† These authors contributed equally to this work.

**Abstract:** Alzheimer's disease (AD) is a specific neurodegenerative disease. This study adopts single-chain variable fragments (scFvs) as a potential immunotherapeutic precursor for AD. According to the remarkable effects of monoclonal antibodies, such as the depolymerization or promotion of A $\beta$ 42 efflux by Crenezumab, Solanezumab, and 12B4, it is attractive to prepare corresponding scFvs targeting amyloid- $\beta$ -42 protein (A $\beta$ 42) and investigate their biological activities. Crenezumab-like scFv (scFv-C), Solanezumab-like scFv (scFv-S), and 12B4-like scFv (scFv-12B4) were designed and constructed. The thermal stabilities and binding ability to A $\beta$ 42 of scFv-C, scFv-S, and scFv-12B4 were evaluated using unfolding profile and enzyme-linked immunosorbent assay. As the results indicated that scFv-C could recognize A $\beta$ 42 monomer/oligomer and promote the disaggregation of A $\beta$ 42 fiber as determined by the Thioflavin-T assay, the potential mechanism of its interaction with A $\beta$ 42 was investigated using molecular dynamics analysis. Interactions involving hydrogen bonds and salt bonds were predicted between scFv-C and A $\beta$ 42 pentamer, suggesting the possibility of inhibiting further aggregation of A $\beta$ 42. The successfully prepared scFvs, especially scFv-C, with favorable biological activity targeting A $\beta$ 42, might be developed for a potentially efficacious clinical application for AD.

**Keywords:** Alzheimer's disease; amyloid- $\beta$ -42 protein; single-chain variable fragment; monoclonal antibody; molecular dynamics simulation



**Citation:** Fan, X.; Xu, L.; Zhang, J.; Wang, Y.; Wu, Z.; Sun, W.; Yao, X.; Wang, X.; Guan, S.; Shan, Y. Mechanism Exploration of Amyloid- $\beta$ -42 Disaggregation by Single-Chain Variable Fragments of Alzheimer's Disease Therapeutic Antibodies. *Int. J. Mol. Sci.* **2023**, *24*, 8371. <https://doi.org/10.3390/ijms24098371>

Academic Editor: Anna Atlante

Received: 26 March 2023

Revised: 3 May 2023

Accepted: 4 May 2023

Published: 6 May 2023



**Copyright:** © 2023 by the authors. Licensee MDPI, Basel, Switzerland. This article is an open access article distributed under the terms and conditions of the Creative Commons Attribution (CC BY) license (<https://creativecommons.org/licenses/by/4.0/>).

## 1. Introduction

Alzheimer's disease (AD) is a progressive neurodegenerative disease that impairs memory and cognitive judgment [1,2]. In 2019, the number of people living with AD worldwide was estimated at 50 million, and it was listed as the seventh-leading cause of death in 2021 [3]. In such a problematic situation, developing effective prevention methods, sensitive diagnostic methods, and effective treatment programs is urgent. Studies have shown three major pathological features in the brains of patients with AD: plaques formed by the accumulation of amyloid- $\beta$ -42 protein (A $\beta$ 42), tangles formed by aggregation of highly phosphorylated microtubule-binding proteins, and neuron loss [4]. The "A $\beta$  cascade hypothesis" has received the most acceptance, suggesting that soluble A $\beta$ 42 oligomer (A $\beta$ O) is the main neurotoxin responsible for synaptic damage and neuronal death [5–7].

Passive immunotherapy targeting A $\beta$ 42 has emerged as one of the promising treatment strategies [8]. A few monoclonal antibodies (mAb) against A $\beta$ 42 have entered clinical

trials or been approved for marketing [9]. Two phase III clinical trials of Bapineuzumab (NCT00574132 and NCT00575055), developed by Janssen and Pfizer, demonstrated that impaired cerebrovascular integrity occurs during anti-amyloid immunotherapy when amyloid is removed from the vessel wall [10]. Crenezumab, developed by Genentech, has an affinity for A $\beta$ O<sub>2</sub> at least ten times that of A $\beta$ 42 monomers (0.4 to 0.6 vs. 3.0 to 5.0 nM), could block aggregation of monomers in vitro, and could induce depolymerization of existing aggregates [11]. Solanezumab, a humanized murine antibody, was tested in clinical phase I, II, and III studies. The results indicated that Solanezumab might have efficacy in AD through a significant effect on or promotion of A $\beta$ 42 efflux from the central nervous system to the peripheral circulation [12,13]. That analysis saw a trend to improve cognition with Solanezumab in people with mild AD but missed statistical significance [13]. MAb 12B4 targets the residues 3 to 7 of A $\beta$ 42, and it recognizes soluble monomers, oligomers, or insoluble aggregates of A $\beta$  species [14].

A single-chain variable fragment (scFv) is a genetically engineered antibody that contains only the variable regions of the heavy and light chains of an antibody and is linked by flexible hinges [15]. Although anti-amyloid mAb that substantially removes A $\beta$ 42 plaques is associated with an adverse event known as amyloid-related imaging abnormalities (ARIA) with edema, microhemorrhage, or superficial siderosis [16], currently, radiologists can optimally impact the management of patients receiving targeted AD therapies [17]. Furthermore, compared with mAb, scFv has advantages, such as the low molecular weights of scFvs enhance the capacity to pass through the blood–brain barrier. ScFvs are safer than mAbs because scFvs do not contain a crystallizable fraction, which might activate microglia and trigger the complement system. Moreover, scFvs can be widely expressed in the prokaryotic expression system and are readily available [18,19].

In our previous studies, both a 12B4-like scFv (scFv-12B4) targeting A $\beta$ 42 and a thermophilic acylpeptide hydrolase were co-conjugated to gold nanorods. The results showed that the gold nanorod complex could reduce A $\beta$ 42-induced cytotoxicity both in vitro and in vivo [20].

Therefore, scFvs were designed as novel potential therapeutic precursors for AD in this study. Crenezumab-like scFv (scFv-C), Solanezumab-like scFv (scFv-S), and 12B4-like scFv (scFv-12B4) were designed based on the antigen-recognition sequences of corresponding monoclonal antibodies, and their biological activities were characterized. To explore the binding mechanism between scFv-C and A $\beta$ 42, molecular dynamics simulation was applied. Molecular dynamics simulation is a computer simulation method to study the physical movement of macromolecules such as proteins [21,22]. Reasonable initial models were constructed to explore the structure and energy changes of scFvs in exerting their functions by simulating the dynamic process [23,24]. This study might provide a potential therapeutic precursor for AD.

## 2. Results

### 2.1. Construction and Identification of pscFvs

The plasmids (Figure 1a) could be double digested by Nco I and Xho I, and the target band (~5 kb) could be observed after nucleic acid electrophoresis (Figure 1b). The sequencing results were also consistent with expectations, confirming the successful construction of the recombinant pscFvs.

### 2.2. Expression and Purification of scFvs

PscFvs were transformed into BL21(DE3) competent cells, and the ideal IPTG concentration for inducing protein expression is 1 mM at 37 °C for 4 h. The Western blot analysis confirmed the successful expression of scFvs in BL21(DE3) competent cells (Figure 2a).

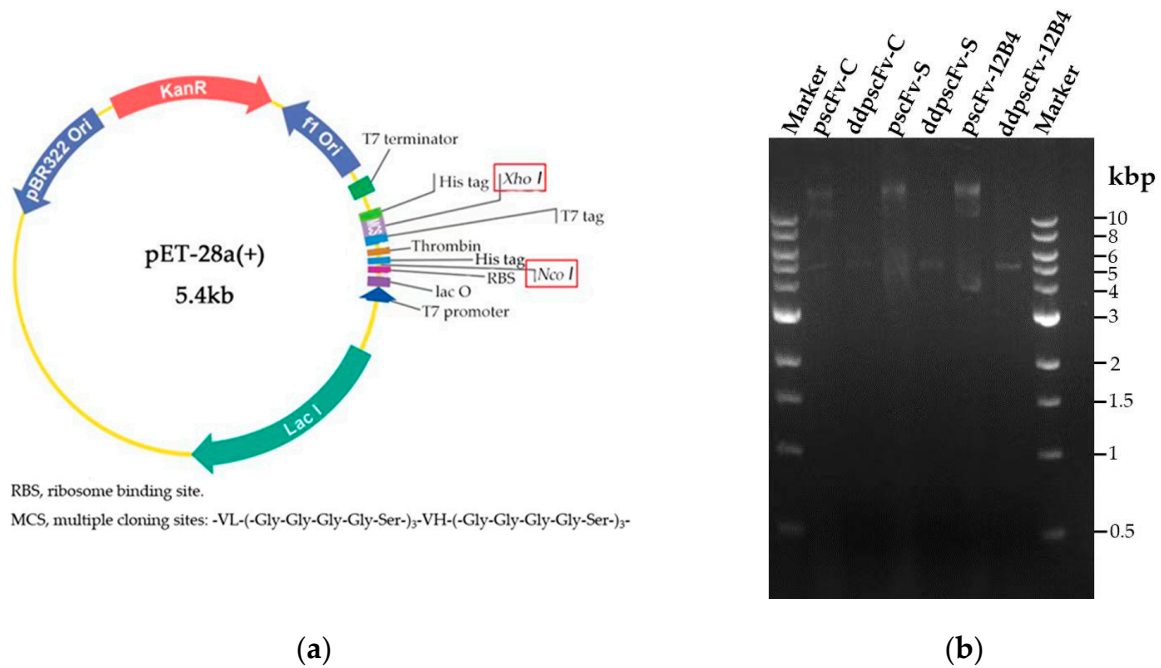


**Figure 1.** The construction and characterization of pscFvs: (a) the plasmid profile of pscFvs, and (b) double digestion of pscFvs.

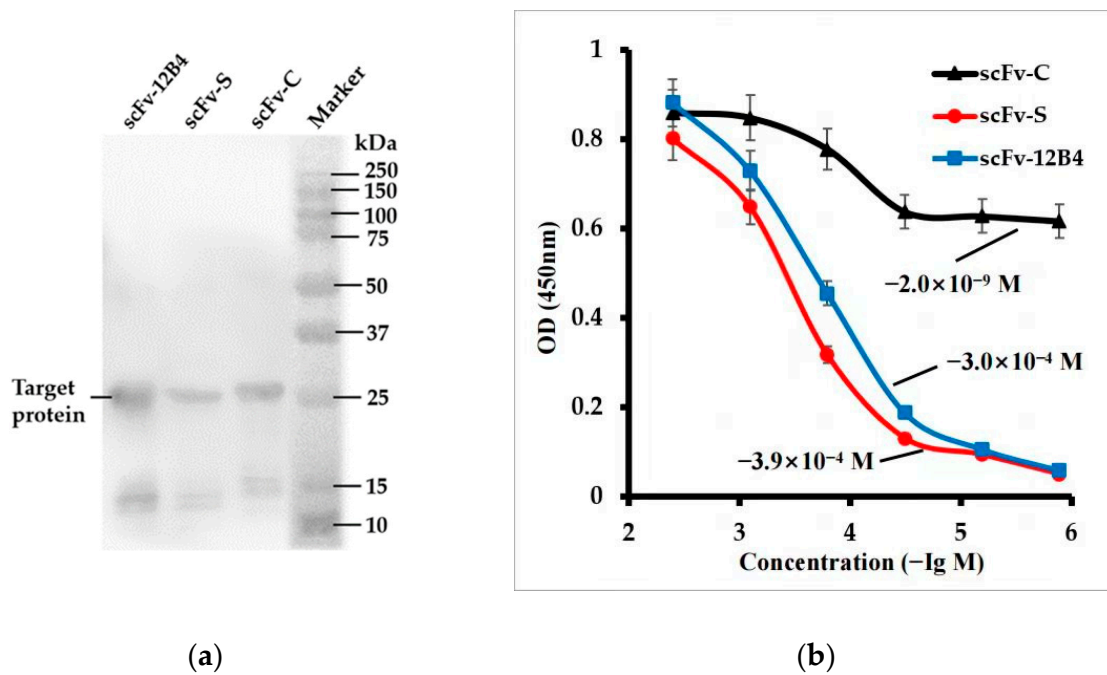


**Figure 2.** Characterization of scFvs activity: (a) Western blotting of scFvs, and (b) the binding activities of scFvs to Aβ42.

**2.3. scFv-C Could Give a Strong Binding Ability with Aβ42**

The binding activities of purified scFv-C, scFv-S, or scFv-12B4 against Aβ42 were determined using ELISA (Figure 2b). The dissociation constant (Kd) corresponds to the scFv concentration at which half of the Aβ42 are occupied at equilibrium [19]. The Kd value of scFv-C was  $\sim 2.0 \times 10^{-9}$  M for Aβ42. The Kd value of scFv-S was  $\sim 3.9 \times 10^{-4}$  M, and that of scFv-12B4 was  $\sim 3.0 \times 10^{-4}$  M. The results indicate that scFv-C has a better binding ability than that of scFv-12B4 or scFv-S.

#### 2.4. scFv Conformation Has Good Thermal Stability

The temperature tolerance of scFvs might allow them to stably recognize and clear A $\beta$ 42. The thermal stabilities of scFvs were evaluated using Nano Temper Tycho under an unfolding condition during the heating process from 35 °C to 95 °C (Figure 3). The results show that the conformations of scFvs could give specific thermal stability. The ratio of 350 nm/330 nm is a measure of the spectral shift of the fluorescence emission profile of tryptophan (Trp) residues, which is used to detect Trp residues exposed on the surface during the unfolding process. Therefore, before the deformation temperature, the conformation of scFvs remained relatively stable and could maintain a complete conformation binding with A $\beta$ 42.

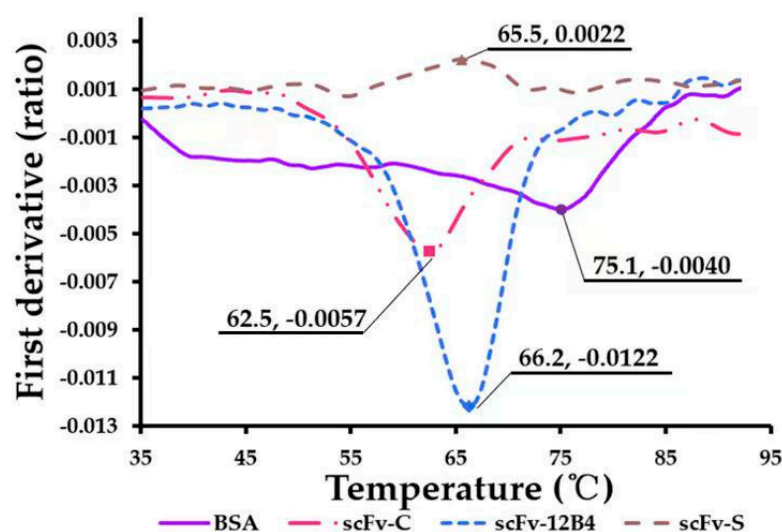


Figure 3. The thermal stability of scFvs.

#### 2.5. scFvs Can Promote Depolymerization of Aggregated A $\beta$ 42

ScFvs can depolymerize aggregated A $\beta$ 42. After incubation for 23 h, the percentage of fluorescence intensity of the mixture treated with scFvs decreased. The results indicated that the amount of aggregated A $\beta$ 42 treated with scFv-C, scFv-S, and scFv-S dropped to 39%, 45%, and 42%, respectively (Figure 4), while the fluorescence intensity of aggregated A $\beta$ 42 dropped to 91%. The above results suggested that scFvs could depolymerize aggregated A $\beta$ 42.

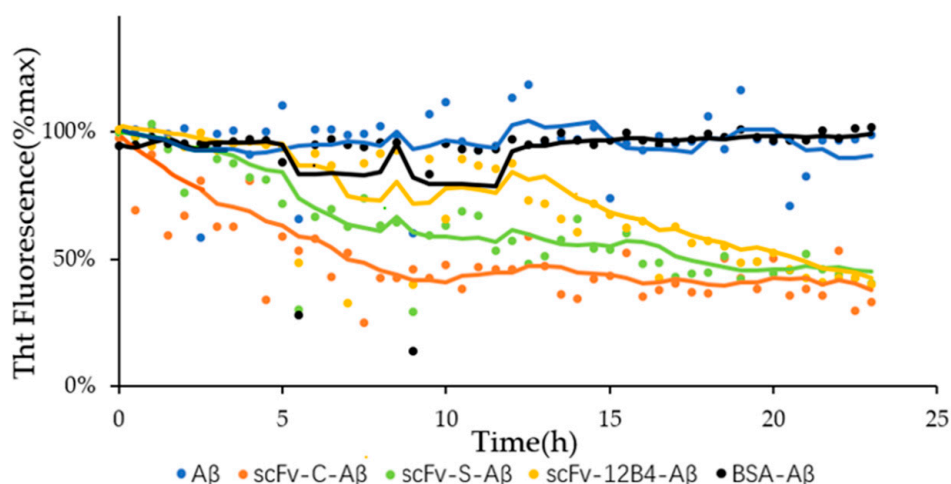


Figure 4. Depolymerization of aggregated A $\beta$ 42 by scFvs. The average of the points were plotted in corresponding color.

## 2.6. Potential Interaction between scFv-C and A $\beta$ <sub>5</sub>

The results indicated that scFv-C could give a better binding ability to A $\beta$ 42 than scFv-12B4 and scFv-S did; therefore, the potential binding modes between scFv-C and A $\beta$ <sub>5</sub>, the A $\beta$ 42 pentamer, were further analyzed via MD. The results showed that the interactions between scFv-C and A $\beta$ <sub>5</sub> were possible through hydrogen bonds and salt bonds. The probabilities of hydrogen bonds of the residues located at the binding interface are shown in Table 1. The possibilities of most hydrogen bonds are between 9% and 20%, where the most considerable probability is the hydrogen bond between ASN178<sup>scFv-C</sup> and GLN15<sup>A $\beta$ 5-mono5</sup>, at 22.77%.

**Table 1.** The hydrogen bonding probability between scFvs and A $\beta$ <sub>5</sub>.

Donor	Acceptor	Probability
ASN58 <sup>scFv-C-Sidechain</sup>	GLU22 <sup>A<math>\beta</math>5-mono2-Sidechain</sup>	12.87%
SER72 <sup>scFv-C-Sidechain</sup>	GLU22 <sup>A<math>\beta</math>5-mono4-Sidechain</sup>	7.92%
THR36 <sup>scFv-C-Sidechain</sup>	GLU22 <sup>A<math>\beta</math>5-mono4-Sidechain</sup>	7.92%
ASN178 <sup>scFv-C-Sidechain</sup>	GLN15 <sup>A<math>\beta</math>5-mono5-Sidechain</sup>	22.77%
SER179 <sup>scFv-C-Sidechain</sup>	GLN15 <sup>A<math>\beta</math>5-mono4-Sidechain</sup>	7.43%
ASN180 <sup>scFv-C-Sidechain</sup>	HIS13 <sup>A<math>\beta</math>5-mono4-Sidechain</sup>	13.86%
GLY73 <sup>scFv-C-Mainchain</sup>	GLU22 <sup>A<math>\beta</math>5-mono4-Sidechain</sup>	5.45%
TYR185 <sup>scFv-C-Sidechain</sup>	GLN15 <sup>A<math>\beta</math>5-mono5-Sidechain</sup>	9.41%
HIS13 <sup>A<math>\beta</math>5-mono5-Sidechain</sup>	SER179 <sup>scFv-C-Sidechain</sup>	9.90%
TYR37 <sup>scFv-C-Sidechain</sup>	VAL18 <sup>A<math>\beta</math>5-mono3-Mainchain</sup>	5.45%
SER57 <sup>scFv-C-Sidechain</sup>	PHE20 <sup>A<math>\beta</math>5-mono2-Mainchain</sup>	11.88%
GLY71 <sup>scFv-C-Mainchain</sup>	GLU22 <sup>A<math>\beta</math>5-mono3-Sidechain</sup>	9.41%
ASN33 <sup>scFv-C-Sidechain</sup>	GLU22 <sup>A<math>\beta</math>5-mono4-Sidechain</sup>	9.41%

The monitoring of the distances of charged residues at the binding interface revealed that the shortest distances between the residues (Lys55<sup>scFv-C</sup>, Arg59<sup>scFv-C</sup>, Arg145<sup>scFv-C</sup>, and Asp226<sup>scFv-C</sup>) on scFv-C and the residues (Asp23<sup>A $\beta$ 5-mono1</sup>, Lys16<sup>A $\beta$ 5-mono2</sup>, Lys16<sup>A $\beta$ 5-mono3</sup>, Glu22<sup>A $\beta$ 5-mono2</sup>, Glu22<sup>A $\beta$ 5-mono3</sup>, and Glu22<sup>A $\beta$ 5-mono4</sup>) on A $\beta$ <sub>5</sub> can be as short as 0.2 nm, as shown in Figure 5 and Figure S2, which may favor salt bond formation.

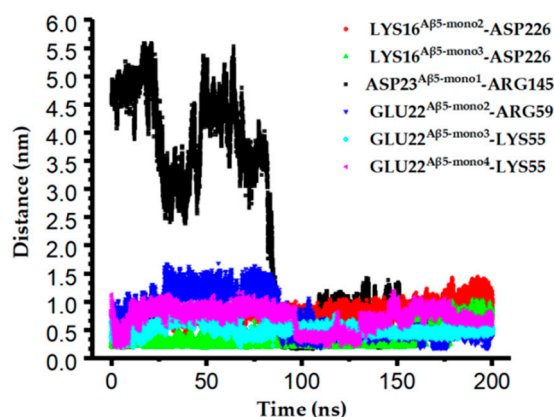


**Figure 5.** The distances of vital charged residues at the binding interface in the scFv-C-A $\beta$ <sub>5</sub> complex.

The binding potential of vital residues was monitored via MM/PBSA. Binding free energy represents the binding potential of residues, and the smaller the value, the stronger the binding potential. In Figure 6a, the binding free energy results indicate that six of the residues of A $\beta$ <sub>5</sub>—Asp23<sup>A $\beta$ 5-mono1</sup>, Glu22<sup>A $\beta$ 5-mono2</sup>, Lys16<sup>A $\beta$ 5-mono2</sup>, Lys16<sup>A $\beta$ 5-mono3</sup>, Glu22<sup>A $\beta$ 5-mono3</sup>, and Glu22<sup>A $\beta$ 5-mono4</sup>—contribute more to the scFv-C and A $\beta$ <sub>5</sub> complex formation than other residues. The significant energetic contributions of the charged residues suggest that salt bonds might play dominant roles. The energy contributions of the residues of scFv-C involved in hydrogen bond formation with A $\beta$ <sub>5</sub> are shown in Figure 6b.

Although the probabilities of hydrogen bonds are not high throughout the simulation, as seen in Table 1, the binding energies of the residues involved in hydrogen bonds still present favorable contributions to scFv-C and A $\beta_5$  complex formation.

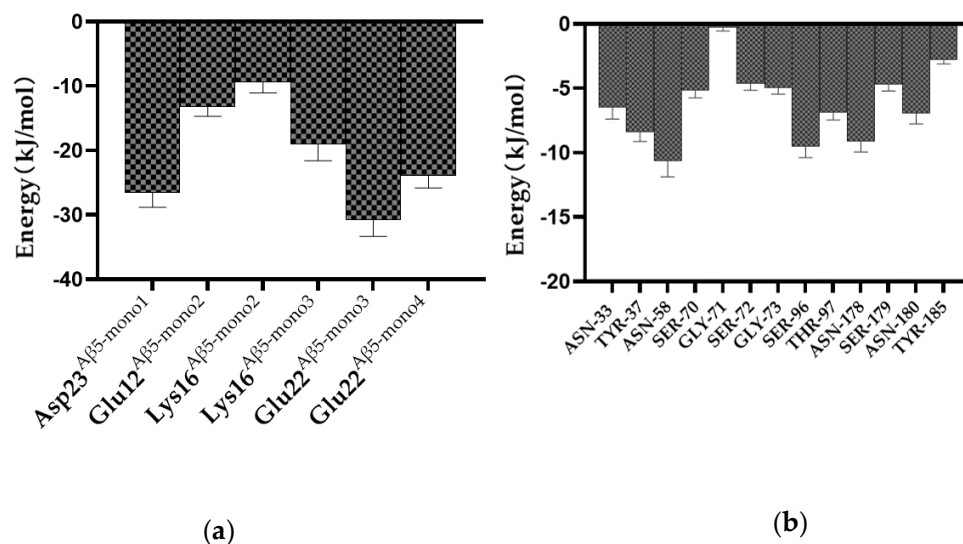


**Figure 6.** The binding energy of vital residues in scFv-C-A $\beta_5$  complex: (a) energies of the residues from A $\beta_5$  involved in salt-bridge formation, and (b) energies of the residues from scFv-C involved in H-bond formation. The error bars represent standard errors.

### 2.7. Simulated Structure Analysis of scFv-C-A $\beta_5$ Complex and A $\beta_5$ System

In this part, the scFv-C-A $\beta_5$  complex system and the A $\beta_5$  system were compared after 200 ns simulation. The results show that after 200 ns simulation, the local disturbance of A $\beta_5$  bound to scFv-C is apparent in the scFv-C-A $\beta_5$  complex system. Notably, the residues Ala21 to Gly29 on each monomer of A $\beta_5$ , indicated by the blue box in Figure 7a, are disturbed. To determine the degree of structural deformation, the root-mean-square deviations (RMSD) of the simulated systems were calculated. RMSD could be employed to evaluate structural perturbation, and the higher the value, the stronger the perturbation.

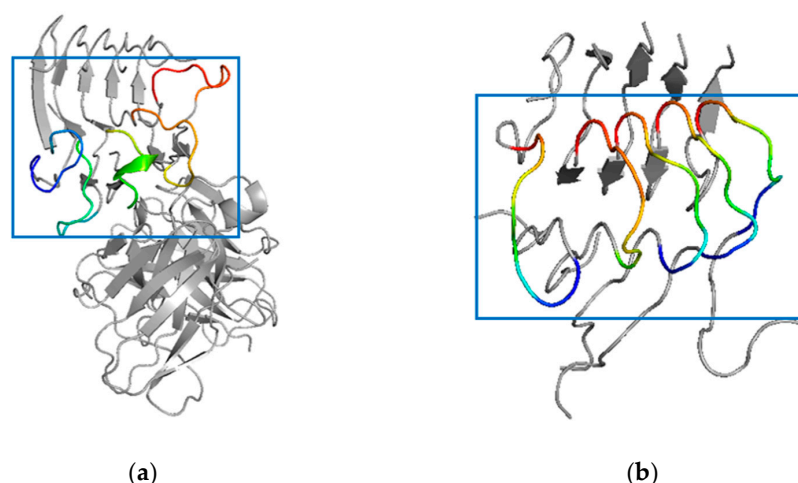


**Figure 7.** Simulated structure of the scFv-C-A $\beta_5$  complex system: (a) structure of scFv-C-A $\beta_5$  complex, and (b) binding surface of A $\beta_5$ .

The RMSD of the Ala21 to Gly29 region of five A $\beta$  monomers, bound and unbound to scFv-C, were obtained and compared. The results showed that the RMSD value of the Ala21 to Gly29 region of mono1, mono3, and mono4 of A $\beta_5$  was significantly increased by

antibody binding, indicating that scFv-C may have the potential to disrupt the structure of A $\beta$ <sub>5</sub> (Figure 8).

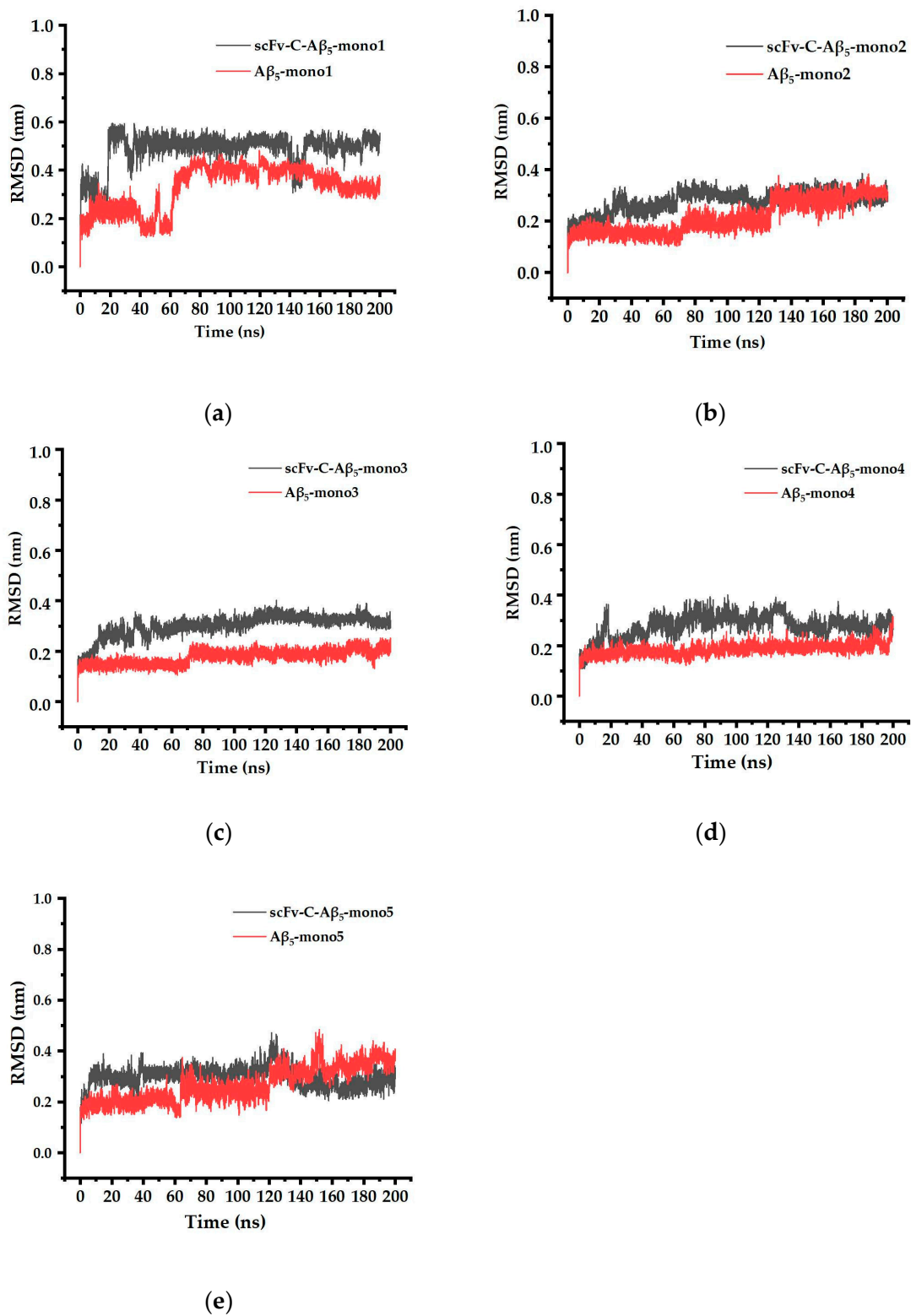


**Figure 8.** The RMSD of the Ala21 to Gly29 region of five A $\beta$  monomers of bound and unbound scFv-C: (a) the RMSD data of scFv-C-A $\beta$ <sub>5</sub>-mono1 and A $\beta$ <sub>5</sub>-mono1; (b) the RMSD data of scFv-C-A $\beta$ <sub>5</sub>-mono2 and A $\beta$ <sub>5</sub>-mono2; (c) the RMSD data of scFv-C-A $\beta$ <sub>5</sub>-mono3 and A $\beta$ <sub>5</sub>-mono3; (d) the RMSD data of scFv-C-A $\beta$ <sub>5</sub>-mono4 and A $\beta$ <sub>5</sub>-mono4; and (e) the RMSD data of scFv-C-A $\beta$ <sub>5</sub>-mono5 and A $\beta$ <sub>5</sub>-mono5.

The secondary structure of the Ala21 to Gly29 region was further monitored. The structural changes of the Ala21 to Gly29 region of A $\beta$ <sub>5</sub> in the scFv-C-A $\beta$ <sub>5</sub> complex system and individual A $\beta$ <sub>5</sub> system were analyzed (Figure 9). After comparing mono1 to mono5 between the bound and unbound systems, the conclusion is that the binding of scFv-C tends to deaggregate A $\beta$ <sub>42</sub> fiber.

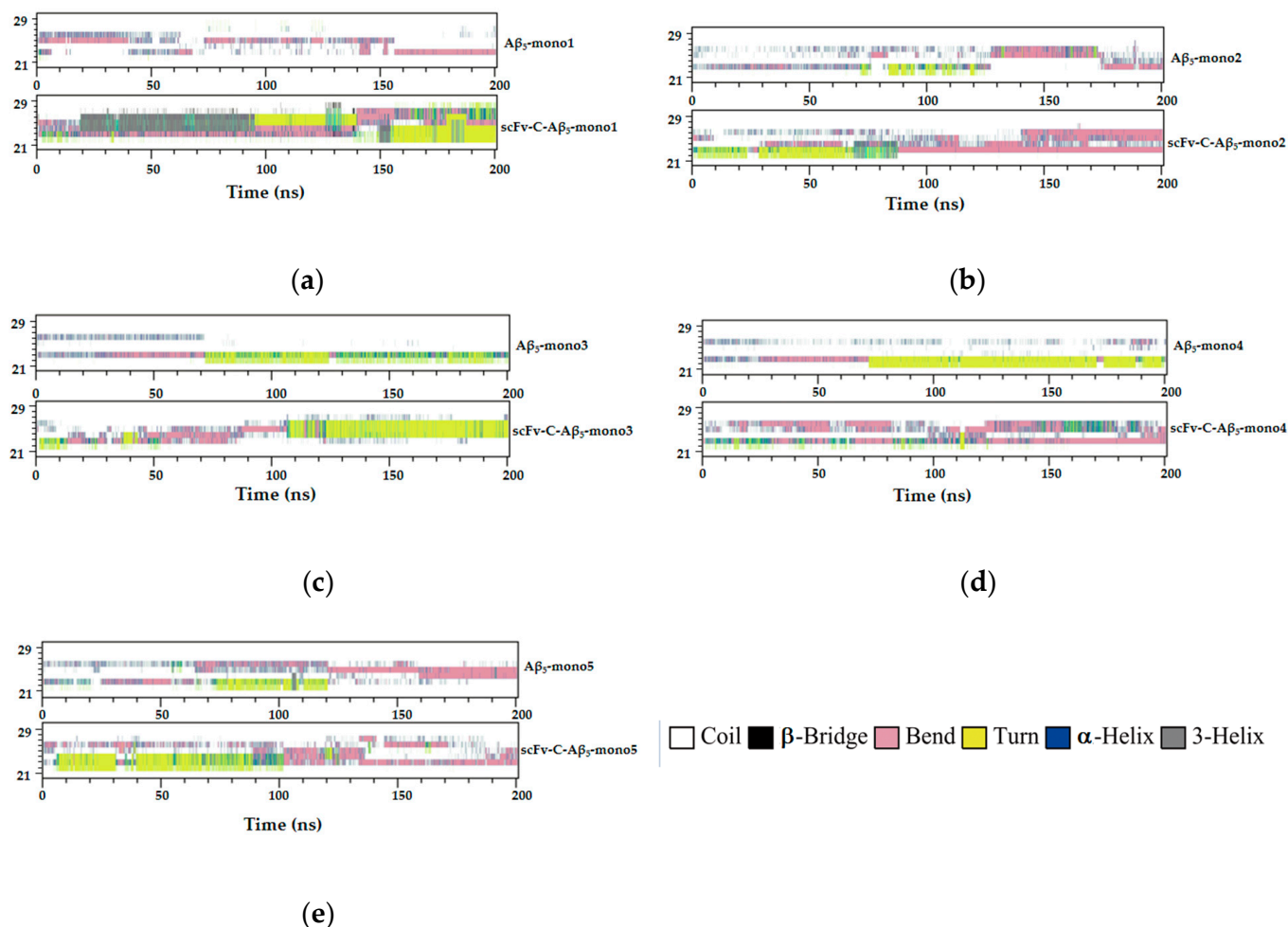


**Figure 9.** Structural transformation of the Ala21-Gly29 region of A $\beta$ <sub>5</sub> in bound and unbound scFv-C systems: (a) structural transformation of scFv-C-A $\beta$ <sub>5</sub>-mono1 and A $\beta$ <sub>5</sub>-mono1; (b) structural transformation of scFv-C-A $\beta$ <sub>5</sub>-mono2 and A $\beta$ <sub>5</sub>-mono2; (c) structural transformation of scFv-C-A $\beta$ <sub>5</sub>-mono3 and A $\beta$ <sub>5</sub>-mono3; (d) structural transformation of scFv-C-A $\beta$ <sub>5</sub>-mono4 and A $\beta$ <sub>5</sub>-mono4; and (e) structural transformation of scFv-C-A $\beta$ <sub>5</sub>-mono5 and A $\beta$ <sub>5</sub>-mono5.

### 3. Discussion

AD is a common neurodegenerative disease, with a rate of up to 50% to 70% of all dementia cases [25]. ScFv, in particular, attaches easily to A $\beta$ Os and fibrils. The passive immune response of scFv with a low molecular weight, is advantageous for crossing the blood-brain barrier [18,19]. Previous studies have indicated that A $\beta$ <sub>42</sub> monomers may be of physiological significance to nerve cells in healthy individuals [19]. An antibody that exclusively recognizes oligomers and fibrils, rather than monomers, is an ideal agent for AD treatment [20].

Three mAbs, Crenezumab, Solanezumab, and 12B4, were chosen in this study. 12B4 displayed the most substantial binding ability to polypeptides and the weakest binding ability to A $\beta$ Os. The reason might be that 12B4 could recognize residues 3 to 7 of A $\beta$ <sub>42</sub>. After its aggregation to form oligomers or fibers, the N-terminal exposure of A $\beta$ <sub>42</sub> is reduced, resulting in a weakened binding ability of antibodies. Solanezumab, which only

binds soluble monomers, recognizes residues 13 to 24 of A $\beta$ 42 [26]. Crenezumab recognizes residues 13 to 24 of A $\beta$ 42 and has a high affinity for the oligomeric form [26–28]. Because of the distinct abilities of these mAbs, corresponding scFvs, scFv-C, scFv-S, and scFv-12B4 were designed and constructed. Their thermal stabilities and binding abilities to A $\beta$ 42 were characterized.

The results obtained using Tycho detect the thermal denaturation of proteins based on fluorescence changes during the heating process (from 35 °C to 95 °C) [29]. According to the instructions, during detection, the ratio of 330nm/350nm measures the spectral displacement of Trp residues' fluorescence emission profile. In the folded state, Trp is usually buried in the hydrophobic nucleus of the protein and exposed to the surface during unfolding. This phenomenon leads to changes in emission intensity and the emission peak wavelength of sample fluorescence, which appears as an inflection point in the unfolded profile and is termed inflection temperature (Ti) [30,31]. The Ti (°C) was 75.3, 62.5, 65.5, and 66.2 for BSA, scFv-C, scFv-S, and scFv-12B4, respectively. These results confirmed that scFvs were thermally stable, and, thus, scFvs could remain in a relatively stable conformation.

Kd represents the affinity of a compound to its target, and the smaller the value, the stronger the affinity [19]. The results from the ELISA showed that scFvs had a high affinity to A $\beta$ 42. Ultsch et al. used surface plasmon resonance to detect the affinity of Crenezumab for A $\beta$ 42 monomers. The full-length IgG4 exhibited a Kd range of 3.0–5.0 nM for A $\beta$ 42 monomers [11]. The results of this study indicated that scFv-C had a better binding ability than scFv-12B4 or scFv-S. ScFv-C also showed a more vital binding ability to A $\beta$ 42 monomer than Crenezumab did.

To our knowledge, Crenezumab remains the only antibody that targets the mid-region of A $\beta$ 42 peptide and binds to multiple aggregated forms with dissociating effects [16]. The binding ability of scFv-C is the strongest among the scFvs; furthermore, scFv-C disaggregates aggregated A $\beta$ 42. Therefore, scFv-C was chosen for further molecular simulations to gain insight into this capability.

Molecular dynamics simulations of scFv-C-A $\beta$ 5 were performed to obtain more information than the static X-ray crystal structure [15]. The RMSD of backbone atoms was calculated to evaluate the simulation's convergence to equilibrium and structural stability [32]. The more significant the RMSD is, the greater the deviation of the target molecule from the reference molecule. The RMSD values of the Ala21 to Gly29 region of mono1, mono3, and mono4 of A $\beta$ 5 were significantly increased by antibody binding, indicating that scFv-C may have the potential to disrupt the structure of A $\beta$ 5. In addition, it can be observed in Figure 4 that after incubation for 23 h, the fluorescence intensity of the A $\beta$  fiber mixture treated with scFv-C decreases to 39%, which can also imply the deaggregation effect of scFv-C on the formed A $\beta$ 42 fiber.

We measured the secondary structure distribution in the scFv-C-A $\beta$ 5 and A $\beta$ 5 systems. In the system of scFv-C-A $\beta$ 5, the Ala21 to Gly29 region of the A $\beta$ 5 adopts diverse structures, including turn structure, bend structure, 3-helical structure, and random coil. Since helical structures are highly distributed only in soluble A $\beta$  species, this may explain the ability of scFv-C to recognize soluble A $\beta$ 42 monomers.

A $\beta$ 42 is one of the essential substances that cause AD. ScFvs have a high affinity for A $\beta$ 42, and the Kd value of scFv-C is about  $2.0 \times 10^{-9}$  M for A $\beta$ 42. In addition, scFv-C conformation has specific thermal stability and maintains good stability and activity in the range of human body temperature. A molecular simulation experiment was performed to explore the binding ability of scFv-C and A $\beta$ 42 pentamer from multiple perspectives. ScFv-C can bind to monomers, oligomers, and fibrous A $\beta$ 42. After binding, there is a tendency for it to depolymerize aggregated A $\beta$ 42. In addition, ScFv-C forms hydrogen bonds and salt bonds to prevent A $\beta$ 42 from further aggregation. This further provides insight into its potential role in AD. In future experiments, scFv-C might be employed to treat AD model mice of different ages and explore the effects of scFv-C on the nervous system.

## 4. Materials and Methods

### 4.1. Materials

A $\beta$ 42 was synthesized by GL Biochem (Shanghai, China). Recombinant plasmids were synthesized by GenScript (Nanjing, China). BL21(DE3) competent cells were purchased from TransGen Biotech (Beijing, China). 3,3',5,5'-tetramethylbenzidine (TMB) was purchased from Tiangen Biotech (Beijing, China). Nitrocellulose membrane was purchased from Whatman (Maidstone, UK). Non-pre-stained Protein Marker was purchased from Thermo Fisher (Rockford, USA). Horseradish peroxidase-labeled (HRP-labeled) goat anti-human IgG (H + L) was purchased from Sino Biological (Beijing, China). Anti-His-tag monoclonal antibody was purchased from Invitrogen (Carlsbad, CA, USA). Protein Marker was purchased from Bio-Rad (CA, USA). Mouse monoclonal antibody,  $\beta$ -Amyloid (B-4), recognizing A $\beta$ 42 was purchased from Santa Cruz Biotechnology, INC.

### 4.2. Methods

#### 4.2.1. Construction of scFv Plasmids (pscFvs)

Amino acid sequences of scFvs were searched from the Research Collaboratory of the Structural Bioinformatics Protein Data Bank (RCSB PDB). The sequences of scFvs are shown in Table S1. Crenezumab (PDB code 5VZY), Solanezumab (PDB code 4XXD), and 12B4 (PDB code 3IFP) could target the residues from 13 to 24, from 13 to 28, and from 3 to 7 of A $\beta$ 42, respectively. The light-chain variable region (VL) and heavy-chain variable region (VH) are connected by a linker, (-Gly-Gly-Gly-Gly-Ser)<sub>3</sub>. The restriction sites of Xho I and Nco I were constructed on the pET28a vector. The recombinant plasmids were optimized and synthesized by Shanghai Kingsley Company.

#### 4.2.2. Prokaryotic Expression of scFvs

The recombinant pscFvs were transformed into BL21(DE3) competent cells, and a single colony was selected and inoculated overnight in 3 mL of Luria-Bertani (LB) medium containing kanamycin (30  $\mu$ g/mL) at 37 °C with constant agitation (220 rpm). The next day, these growths were transferred into 30 mL of LB medium and grown to an optical density (OD) of 0.6–0.8 at 600 nm. Isopropyl- $\beta$ -d-thiogalactopyranoside (IPTG) was added to a final concentration of 1 mM. The samples were harvested after induction culture at 37 °C for 4 h. At the same time, bacteria without induction were broken by ultrasound and centrifuged. The supernatant and precipitate were collected and identified using sodium dodecyl sulfate–polyacrylamide gel electrophoresis (SDS-PAGE).

#### 4.2.3. Purification of Recombinant scFvs

The supernatant was discarded by centrifugation to collect the precipitate, resuspended in 20 mL of 8 M urea (0.05 M Tris, 0.15 M NaCl, pH 8.0, and 8 M urea). After ultrasonic crushing, inclusion bodies were collected by centrifugation at 10,000 r/min at 4 °C for 20 min, and the supernatant was discarded. The inclusion bodies were dissolved in 8 M urea. After centrifugation at 10,000 rpm and 4 °C for 20 min, the supernatant was filtered using a 0.45  $\mu$ m filter and purified using an affinity His-Trap™ column (GE Healthcare, Piscataway, NJ, USA). The proteins were eluted using imidazole, dialyzed, and concentrated. Finally, the purified proteins were obtained and stored at –20 °C.

#### 4.2.4. Characterization of scFvs Based on Western Blotting

ScFv purity was assessed using SDS-PAGE. The samples were boiled in a SDS sample-loading buffer containing dithiothreitol. The ScFvs were electrophoresed on a 12% SDS-PAGE gel, followed by blotting, and then analysis was performed using Western blotting with an anti-His-tag monoclonal antibody (Invitrogen, Carlsbad, CA, USA). Western blotting was visualized using a ECL Plus substrate (Tanon Science and Technology, Shanghai, China).

#### 4.2.5. Characterization of scFvs' Binding Activities Based on Enzyme-Linked Immunosorbent Assay (ELISA)

ScFvs were diluted from 4  $\mu\text{M}$  to 1.28 nM in a 1:5 dilution ratio. The ELISA was performed in 96-well plates coated with scFvs (100  $\mu\text{L}$ /well) at 4  $^{\circ}\text{C}$  overnight. Each well was added with A $\beta$ 42 to 3  $\mu\text{M}$ . After incubating at 37  $^{\circ}\text{C}$  for 1 h, the plates were washed three times with PBST.  $\beta$ -Amyloid (B-4) (1:2000) was added to the wells for 2 h at 37  $^{\circ}\text{C}$ . After washing with PBST, HRP-labeled goat anti-human IgG (H+L) (1:4000) was added into each well. After incubating at 37  $^{\circ}\text{C}$  for 1 h, 3,3',5,5'-tetramethylbenzidine solution (Tiangen Biotech, Beijing, China) was added to develop color, and color development was stopped using 2 M  $\text{H}_2\text{SO}_4$ . The absorbance at 450 nm was measured using an iMark™ Microplate Reader (Bio-TEK, Winooski, VT, USA).

#### 4.2.6. Characterization of scFvs' Thermal Stability

The thermal stability of scFv-C, scFv-S, and scFv-12B4 was detected using Tycho NT.6 (NanoTemper Technologies, Munich, Germany). Bovine serum albumin (BSA) was used as a control.

#### 4.2.7. Promoting Effect on Depolymerization of Aggregated A $\beta$ 42

Aggregated A $\beta$ 42 was prepared as we previously described [33]. A total of 3  $\mu\text{L}$  of aggregated A $\beta$ 42 (1 mg/mL in 10 mM NaOH) and 1.6  $\mu\text{L}$  of Thioflavin-T (THT) solution (5 mM) was mixed in opaque 96-well plates overnight, and aggregated A $\beta$ 42 was allowed to form. The ScFvs were mixed in, and the plates were filled to 150  $\mu\text{L}$  with a buffer (pH 7.0) containing 10 mM phosphate buffer (PB) and 500 mM NaCl. Fluorescence was detected every hour using a fluorescence microplate reader (Thermo Fisher Scientific, Waltham, MA, USA) at an excitation/emission wavelength of 485 nm/535 nm, respectively [33].

#### 4.2.8. Three-Dimensional Structure Construction of scFv-C and A $\beta$ 42 Pentamer (A $\beta$ <sub>5</sub>) Complex System

In order to predict the potential mechanism of binding between scFv-C and A $\beta$ <sub>5</sub>, the 3D structure of scFv-C was constructed using the Swiss Model web platform [32,34–37]. The template for homology modeling was selected from the RCSB PDB with the ID of 3AUV [38]. The complex containing scFv-C and A $\beta$ <sub>5</sub> was obtained using the HADDOCK docking program [39]. According to the position of the complementarity-determining regions (CDR) of the antibody in the template structure, the docking binding-site residues were determined as CDR-L1 (ssqslvysn), CDR-L2 (qlliyvs), CDR-L3 (thvp), CDR-H1 (gftfssygmwv), CDR-H2 (ggst), and CDR-H3 (ycasgdyw). A $\beta$ <sub>5</sub> was selected to participate in docking with scFv-C. The structure of the scFv-C and its comparison with the template is shown in Figure S1.

#### 4.2.9. Molecular Dynamics Simulation

Molecular simulation sampling was carried out for the scFv-C-A $\beta$ <sub>5</sub> complex systems and individual A $\beta$ <sub>5</sub> systems, respectively. The complex systems were subjected to molecular dynamics simulation with periodic boundary conditions using the Gromacs 5.1.5 software package with a simple point-charge water model [40–42]. The Gromos 54 A7 force field was applied to describe scFv-C and A $\beta$ <sub>5</sub> [43].

First, the energies of the complex systems were relaxed with steepest-descent energy minimization to eliminate steric clashes or incorrect geometry. After that, 100 ps NVT (constant Number of particles, Volume, and Temperature) and NPT (constant Number of particles, Pressure, and Temperature) were alternately operated with position restraints on scFv-C and A $\beta$ <sub>5</sub> to relax the solvent molecules in two phases [44,45]. The solvent molecules were equilibrated with a fixed protein at 310 K, and the initial velocities were chosen from a Maxwellian distribution. Subsequently, scFv-C and A $\beta$ <sub>5</sub> were relaxed stepwise and heated to 310 K. The long-range electrostatic interactions were described using the particle mesh Ewald algorithm, with an interpolation order of 4, a grid spacing of 0.16 nm,

and a Coulomb cutoff distance of 1.0 nm [46]. Temperature-and-pressure coupling types were set using V-rescale and the Parrinello–Rahman method, respectively [47]. In the NVT ensemble, the temperature of the systems reached a plateau at the desired value (reference temperature = 310 K; time constant = 0.1 ps). In addition, the equilibration of pressure (reference pressure = 1.0 bar; time constant = 2.0 ps) was performed under the NPT ensemble. The equilibrated ensembles were subjected to molecular dynamics simulations conducted for 200 ns employing the LINear Constraint Solver (LINCS) and SETTLE algorithm for bond constraints and geometry of water molecules. The 200 ns molecular dynamics simulations were initiated for collecting data with a time step of 2 fs, and coordinates were saved every 2 ps [48,49].

#### 4.2.10. Binding Energy Calculation

The molecular mechanics Poisson–Boltzmann surface area method (MM/PBSA) is applied as a scoring function in computational drug design to estimate free energies in biomolecular interactions [50–52]. Using the command “gmx\_mmpbsa”, the binding free energy of a complex was calculated from 200 snapshots extracted from the 200 ns MD trajectory. Furthermore, the binding energy was decomposed on a per-residue basis to analyze the individual energy contributions of each residue to the scFv-C-A $\beta$ <sub>5</sub> interaction.

**Supplementary Materials:** The supporting information can be downloaded at <https://www.mdpi.com/article/10.3390/ijms24098371/s1>.

**Author Contributions:** Conceptualization and Resources, Y.S. and S.G.; methodology, X.Y., Y.S., S.G. and X.W.; software, Z.W. and S.G.; formal analysis, X.F., L.X. and J.Z.; data curation, W.S. and Y.S.; writing—original draft preparation, X.F., L.X. and J.Z.; writing—review and editing, Y.W., Y.S. and S.G. All authors have read and agreed to the published version of the manuscript.

**Funding:** This research was funded by the National Natural Science Foundation of China, grant number: 31770996; the Youth Program of the National Natural Science Foundation of China, grant number 31901062; the Jilin Province Science and Technology Development Projects, grant number 20210204197YY; the Changchun City Science and Technology Development Projects, grant number 21ZY15 and the Jilin Province Science and Technology Development Plan Projects, grant number YDZJ202301ZYTS341.

**Institutional Review Board Statement:** The study does not require ethical approval.

**Informed Consent Statement:** Not applicable.

**Data Availability Statement:** The authors confirm that the data supporting the findings of this study are available within the article and its Supplementary Materials.

**Conflicts of Interest:** The authors declare no conflict of interest.

#### Abbreviation

amyloid beta protein (A $\beta$ ); amino acid 1–42 of amyloid- $\beta$ -42 (A $\beta$ 42); A $\beta$ 42 oligomer (A $\beta$ O); A $\beta$ 42 pentamer (A $\beta$ <sub>5</sub>); Alzheimer’s disease (AD); thermophilic acylpeptide hydrolase (APH); amyloid-related imaging abnormalities (ARIA); bovine serum albumin (BSA); complementarity-determining regions (CDR); crystallizable fraction (Fc); horseradish peroxidase-labeled (HRP-labeled); isopropyl- $\beta$ -d-thiogalactopyranoside (IPTG); equilibrium dissociation constant (K<sub>d</sub>); Luria-Bertani (LB); LINear Constraint Solver (LINCS); monoclonal antibody (mAb); molecular dynamics (MD); molecular mechanics Poisson–Boltzmann surface area method (MM/PBSA); constant Number of particles, Pressure, and Temperature (NPT); constant Number of particles, Volume, and Temperature (NVT); presenilin 1 (PSEN1); phosphate-buffered saline (PBS); PBS containing 0.5 percent Tween 20 (PBST); Research Collaboratory for Structural Bioinformatics (RCSB); single-chain variable fragment (scFv); Crenezumab-like scFv (scFv-C); Solanezumab-like scFv (scFv-S); 12B4-like scFv (scFv-12B4); sodium dodecyl sulfate–polyacrylamide gel electrophoresis (SDS-PAGE); Thioflavin-T (THT); inflection temperature (T<sub>i</sub>); 3,3,5,5’-tetramethylbenzidine (TMB); tryptophan (Trp).

## References

1. Manca, R.; Pardiñas, A.F.; Venneri, A. Alzheimer's Disease Neuroimaging Initiative. The neural signatures of psychoses in Alzheimer's disease: A neuroimaging genetics approach. *Eur. Arch. Psychiatry. Clin. Neurosci.* **2023**, *273*, 253–267. [[CrossRef](#)] [[PubMed](#)]
2. Lopes, C.R.; Silva, J.S.; Santos, J.; Rodrigues, M.S.; Madeira, D.; Oliveira, A.; Moreira-de-Sá, A.; Lourenço, V.S.; Gonçalves, F.Q.; Silva, H.B.; et al. Downregulation of Sirtuin 1 does not account for the impaired long-term potentiation in the prefrontal cortex of female APPswe/PS1dE9 mice modelling Alzheimer's disease. *Int. J. Mol. Sci.* **2023**, *24*, 6968. [[CrossRef](#)] [[PubMed](#)]
3. Gaugler, J.; James, B.; Johnson, T.; Reimer, J.; Solis, M.; Weuve, J.; Buckley, R.F.; Hohman, T.J. 2022 Alzheimer's disease facts and figures. *Alzheimers Dement.* **2022**, *18*, 700–789. [[CrossRef](#)]
4. Xu, C.; Zhao, L.; Dong, C. A review of application of A $\beta$ 42/40 ratio in diagnosis and prognosis of Alzheimer's disease. *J. Alzheimers Dis.* **2022**, *90*, 495–512. [[CrossRef](#)]
5. Johnson, N.R.; Wang, A.C.; Coughlan, C.; Sillau, S.; Lucero, E.; Viltz, L.; Markham, N.; Allen, C.; Dhanasekaran, A.R.; Chial, H.J.; et al. Imipramine and olanzapine block apoE4-catalyzed polymerization of A $\beta$  and show evidence of improving Alzheimer's disease cognition. *Alzheimers Res. Ther.* **2022**, *14*, 88. [[CrossRef](#)]
6. Bivona, G.; Iemmolo, M.; Piccoli, T.; Agnello, L.; Lo Sasso, B.; Ciaccio, M.; Gherzi, G. High cerebrospinal fluid CX3CL1 levels in Alzheimer's disease patients but not in non-Alzheimer's disease dementia. *J. Clin. Med.* **2022**, *11*, 5498. [[CrossRef](#)]
7. Kabir, E.R.; Chowdhury, N.M.; Yasmin, H.; Kabir, M.T.; Akter, R.; Perveen, A.; Ashraf, G.M.; Akter, S.; Rahman, M.H.; Sweilam, S.H. Unveiling the potential of polyphenols as anti-amyloid molecules in Alzheimer's disease. *Curr. Neuropharmacol.* **2022**, *14*, 787–807. [[CrossRef](#)]
8. Martinez, B.; Peplow, V.P. Amelioration of Alzheimer's disease pathology and cognitive deficits by immunomodulatory agents in animal models of Alzheimer's disease. *Neural Regen. Res.* **2019**, *14*, 1158–1176.
9. Cummings, J.L.; Goldman, D.P.; Simmons-Stern, N.R.; Ponton, E. The costs of developing treatments for Alzheimer's disease: A retrospective exploration. *Alzheimers Dement.* **2022**, *18*, 469–477. [[CrossRef](#)]
10. Brashear, H.R.; Ketter, N.; Bogert, J.; Di, J.; Salloway, S.P.; Sperling, R. Clinical evaluation of amyloid-related imaging abnormalities in bapineuzumab phase III studies. *J. Alzheimer's Dis.* **2018**, *66*, 1409–1424. [[CrossRef](#)]
11. Ultsch, M.; Li, B.; Maurer, T.; Mathieu, M.; Adolfsson, O.; Muhs, A.; Pfeifer, A.; Pihlgren, M.; Bainbridge, T.W.; Reichelt, M.; et al. Structure of crenezumab complex with A $\beta$  shows loss of  $\beta$ -hairpin. *Sci. Rep.* **2016**, *6*, 39374. [[CrossRef](#)] [[PubMed](#)]
12. Sink, K.; Warren, F.; Smith, J.; Schneider, A.; Fuji, R.N.; Quartino, A.; Mackey, H.; Rabbia, M.; Yule, S.; Fontoura, P.; et al. P1-046: Baseline characteristics from cread2: A phase III trial of crenezumab in early (prodromal-to-mild) Alzheimer's disease. *Alzheimers Dement.* **2019**, *15*, P250. [[CrossRef](#)]
13. Doody, R.S.; Thomas, R.G.; Farlow, M.; Iwatsubo, T.; Vellas, B.; Joffe, S.; Kieburtz, K.; Raman, R.; Sun, X.; Aisen, P.S.; et al. Phase 3 trials of solanezumab for mild-to-moderate Alzheimer's disease. *N. Engl. J. Med.* **2014**, *370*, 311–321. [[CrossRef](#)]
14. Bard, F.; Barbour, R.; Cannon, C.; Carretto, R.; Fox, M.; Games, D.; Guido, T.; Hoenow, K.; Hu, K.; Johnson-Wood, K.; et al. Epitope and isotype specificities of antibodies to beta-amyloid peptide for protection against Alzheimer's disease-like neuropathology. *Proc. Natl. Acad. Sci. USA* **2003**, *100*, 2023–2028. [[CrossRef](#)]
15. Ahmad, Z.A.; Yeap, S.K.; Ali, A.M.; Ho, W.Y.; Alitheen, N.B.; Hamid, M. ScFv antibody: Principles and clinical application. *Clin. Dev. Immunol.* **2012**, *2012*, 980250. [[CrossRef](#)] [[PubMed](#)]
16. Sotoudeh, H.; Alizadeh, M.; Shahidi, R.; Shobeiri, P.; Love, N.; Singhal, A. Subcortical signal alteration of corticospinal tracts. A radiologic manifestation of ARIA: A case report. *Radiol. Case Rep.* **2022**, *18*, 275–279. [[CrossRef](#)]
17. Roytman, M.; Mashriqi, F.; Al-Tawil, K.; Schulz, P.E.; Zaharchuk, G.; Benzinger, T.L.S.; Franceschi, A.M. Amyloid-related imaging abnormalities: An update. *AJR Am. J. Roentgenol.* **2023**, *220*, 562–574. [[CrossRef](#)]
18. Sun, Z.T.; Ma, C.; Li, G.J.; Zheng, J.Y.; Hao, Y.T.; Yang, Y.; Wang, X. Application of antibody fragments against A $\beta$  with emphasis on combined application with nanoparticles in Alzheimer's disease. *Front. Pharmacol.* **2021**, *12*, 654611. [[CrossRef](#)]
19. Zhang, Y.; Qian, L.; Kuang, Y.; Liu, J.; Wang, D.; Xie, W.; Zhang, L.; Fu, L. An adeno-associated virus-mediated immunotherapy for Alzheimer's disease. *Mol. Immunol.* **2022**, *144*, 26–34. [[CrossRef](#)]
20. Liu, D.; Li, W.; Jiang, X.; Bai, S.; Liu, J.; Liu, X.; Shi, Y.; Kuai, Z.; Kong, W.; Gao, R. Using near-infrared enhanced thermozyme and scFv dual-conjugated Au nanorods for detection and targeted photothermal treatment of Alzheimer's disease. *Theranostics* **2019**, *9*, 2268–2281. [[CrossRef](#)]
21. Zhou, K.; Liu, B. *Molecular Dynamics Simulation: Fundamentals and Applications*; Academic Press: Cambridge, MA, USA, 2022.
22. Schmidt, A.G.; Xu, H.; Khan, A.R.; O'Donnell, T.; Khurana, S.; King, L.R.; Manischewitz, J.; Golding, H.; Suphaphiphat, P.; Carfi, A.; et al. Preconfiguration of the antigen-binding site during affinity maturation of a broadly neutralizing influenza virus antibody. *Proc. Natl. Acad. Sci. USA* **2013**, *110*, 264–269. [[CrossRef](#)] [[PubMed](#)]
23. Zhou, B.R.; Bai, Y. Preparation of scFv stabilized chromatosomes for single-particle cryo-EM structure determination. *STAR Protoc.* **2021**, *2*, 100396. [[CrossRef](#)] [[PubMed](#)]
24. Moser, A.C.; Trenhaile, S.; Frankenberg, K. Studies of antibody-antigen interactions by capillary electrophoresis: A review. *Methods* **2018**, *146*, 66–75. [[CrossRef](#)]
25. Dulewicz, M.; Kulczyńska-Przybik, A.; Mroczo, P.; Kornhuber, J.; Lewczuk, P.; Mroczo, B. Biomarkers for the diagnosis of Alzheimer's disease in clinical practice: The role of CSF biomarkers during the evolution of diagnostic criteria. *Int. J. Mol. Sci.* **2022**, *23*, 8598. [[CrossRef](#)]

26. Bouter, Y.; Lopez Noguerola, J.S.; Tucholla, P.; Crespi, G.A.; Parker, M.W.; Wiltfang, J.; Miles, L.A.; Bayer, T.A. Abeta targets of the biosimilar antibodies of Bapineuzumab, Crenezumab, Solanezumab in comparison to an antibody against N-truncated Abeta in sporadic Alzheimer disease cases and mouse models. *Acta Neuropathol.* **2015**, *130*, 713–729. [[CrossRef](#)] [[PubMed](#)]
27. Lin, L.; Madrasi, K.; Abdul, H.; Young, C.; Park, J.; Burke, J.; Apgar, J.; Hua, F.; Gruenbaum, L. Quantitative systems pharmacology model of amyloid beta and plaque dynamics in Alzheimer's disease upon treatment with Crenezumab, Solanezumab, and Bapineuzumab. *Clin. Pharmacol. Ther.* **2019**, *105*, S104.
28. Imbimbo, B.P.; Triaca, V.; Imbimbo, C.; Nisticò, R. Investigational treatments for neurodegenerative diseases caused by inheritance of gene mutations: Lessons from recent clinical trials. *Neural Regen. Res.* **2023**, *18*, 1679–1683. [[CrossRef](#)] [[PubMed](#)]
29. Kojic, M.; Gaik, M.; Kiska, B.; Salerno-Kochan, A.; Hunt, S.; Tedoldi, A.; Mureev, S.; Jones, A.; Whittle, B.; Genovesi, L.A.; et al. Elongator mutation in mice induces neurodegeneration and ataxia-like behavior. *Nat. Commun.* **2018**, *9*, 3195. [[CrossRef](#)]
30. Breitsprecher, D.; Fung, P.A.; Tschammer, N. Improving biosensor assay development by determining sample quality with Tycho NT.6. *Nat. Methods* **2018**, *15*, 298. [[CrossRef](#)]
31. Qiao, Y.; Zhang, Y.; Chen, J.; Jin, S.; Shan, Y. A biepitope, adjuvant-free, self-assembled influenza nanovaccine provides cross-protection against H3N2 and H1N1 viruses in mice. *Nano Res.* **2022**, *15*, 8304–8314. [[CrossRef](#)]
32. Bertoni, M.; Kiefer, F.; Biasini, M.; Bordoli, L.; Schwede, T. Modeling protein quaternary structure of homo- and hetero-oligomers beyond binary interactions by homology. *Sci. Rep.* **2017**, *7*, 10480. [[CrossRef](#)]
33. Sun, D.; Qiao, Y.; Jiang, X.; Li, P.; Kuai, Z.; Gong, X.; Liu, D.; Fu, Q.; Sun, L.; Li, H.; et al. Multiple Antigenic Peptide System Coupled with Amyloid Beta Protein Epitopes As An Immunization Approach to Treat Alzheimer's Disease. *ACS Chem. Neurosci.* **2019**, *10*, 2794–2800. [[CrossRef](#)]
34. Waterhouse, A.; Bertoni, M.; Bienert, S.; Studer, G.; Tauriello, G.; Gumienny, R.; Heer, F.T.; de Beer, T.A.P.; Rempfer, C.; Bordoli, L.; et al. SWISS-MODEL: Homology modelling of protein structures and complexes. *Nucleic Acids Res.* **2018**, *46*, 296–303. [[CrossRef](#)] [[PubMed](#)]
35. Bienert, S.; Waterhouse, A.; de Beer, T.A.; Tauriello, G.; Studer, G.; Bordoli, L.; Schwede, T. The SWISS-MODEL Repository—new features and functionality. *Nucleic Acids Res.* **2017**, *45*, 313–319. [[CrossRef](#)]
36. Guex, N.; Peitsch, M.C.; Schwede, T. Automated comparative protein structure modeling with SWISS-MODEL and Swiss-PdbViewer: A historical perspective. *Electrophoresis* **2009**, *30*, 162–173. [[CrossRef](#)] [[PubMed](#)]
37. Studer, G.; Rempfer, C.; Waterhouse, A.M.; Gumienny, R.; Haas, J.; Schwede, T.; Elofsson, A. QMEANDisCo—distance constraints applied on model quality estimation. *Bioinformatics* **2020**, *36*, 2647. [[CrossRef](#)] [[PubMed](#)]
38. Yu, C.M.; Peng, H.P.; Chen, I.C.; Lee, Y.C.; Chen, J.B.; Tsai, K.C.; Chen, C.T.; Chang, J.Y.; Yang, E.W.; Hsu, P.C.; et al. Rationalization and Design of the Complementarity Determining Region Sequences in an Antibody-Antigen Recognition Interface. *PLoS ONE* **2012**, *7*, e33340. [[CrossRef](#)] [[PubMed](#)]
39. van Zundert, G.C.P.; Rodrigues, J.P.G.L.M.; Trellet, M.; Schmitz, C.; Kastiris, P.L.; Karaca, E.; Melquiond, A.S.J.; van Dijk, M.; de Vries, S.J.; Bonvin, A.M.J.J. The HADDOCK2.2 Web Server: User-Friendly Integrative Modeling of Biomolecular Complexes. *J. Mol. Biol.* **2016**, *428*, 720–725. [[CrossRef](#)] [[PubMed](#)]
40. Hess, B.; van der Vegt, N.F. Hydration thermodynamic properties of amino acid analogues: A systematic comparison of biomolecular force fields and water models. *J. Phys. Chem. B* **2006**, *110*, 17616–17626. [[CrossRef](#)]
41. Hess, B.; Kutzner, C.; van der Spoel, D.; Lindahl, E. GROMACS 4: Algorithms for highly efficient, load-balanced, and scalable molecular simulation. *J. Chem. Theory Comput.* **2008**, *4*, 435–447. [[CrossRef](#)]
42. Safarizadeh, H.; Garkani-Nejad, Z. Molecular docking, molecular dynamics simulations and QSAR studies on some of 2-arylethenylquinoline derivatives for inhibition of Alzheimer's amyloid-beta aggregation: Insight into mechanism of interactions and parameters for design of new inhibitors. *J. Mol. Graph. Model.* **2019**, *87*, 129–143. [[CrossRef](#)]
43. Bachmann, S.J.; Van Gunsteren, W.F. Structural and energetic effects of the use of polarisable water to solvate proteins. *Mol. Phys.* **2015**, *113*, 2815–2828. [[CrossRef](#)]
44. Liu, Y.; Guan, S.; Luo, Z.; Han, F.; Han, W.; Wang, S.; Zhang, H. How different substitution positions of F, Cl atoms in benzene ring of 5-methylpyrimidine pyridine derivatives affect the inhibition ability of EGFR<sup>L858R/T790M/C797S</sup> inhibitors: A molecular dynamics simulation study. *Molecules* **2020**, *25*, 895–920.
45. Pan, Y.; Lu, Z.; Li, C.; Qi, R.; Chang, H.; Han, L.; Han, W. Molecular dockings and molecular dynamics simulations reveal the potency of different inhibitors against Xanthine oxidase. *ACS Omega* **2021**, *6*, 11639–11649. [[CrossRef](#)] [[PubMed](#)]
46. Rampogu, S.; Baek, A.; Park, C.; Son, M.; Parate, S.; Parameswaran, S.; Park, Y.; Shaik, B.; Kim, J.H.; Park, S.J.; et al. Discovery of small molecules that target vascular endothelial growth factor receptor-2 signalling pathway employing molecular modelling studies. *Cells* **2019**, *8*, 269. [[CrossRef](#)] [[PubMed](#)]
47. Pei, P.; Qin, H.; Chen, J.; Wang, F.; He, C.; He, S.; Hong, B.; Liu, K.; Qiao, R.; Fan, H.; et al. Computational design of ultrashort peptide inhibitors of the receptor-binding domain of the SARS-CoV-2 S protein. *Brief. Bioinform.* **2021**, *22*, 243. [[CrossRef](#)] [[PubMed](#)]
48. Sadr, A.S.; Eslahchi, C.; Ghassempour, A.; Kiaei, M. In silico studies reveal structural deviations of mutant profilin-1 and interaction with riluzole and edaravone in amyotrophic lateral sclerosis. *Sci. Rep.* **2021**, *11*, 6849. [[CrossRef](#)]
49. Qian, M.; Guan, S.; Shan, Y.; Zhang, H.; Wang, S. Structural and molecular basis of cellulase Cel48F by computational modeling: Insight into catalytic and product release mechanism. *J. Struct. Biol.* **2016**, *194*, 347–356. [[CrossRef](#)] [[PubMed](#)]

50. Wang, M.; Wong, C.F. Rank-ordering protein-ligand binding affinity by a quantum mechanics/molecular mechanics/Poisson-Boltzmann-surface area model. *J. Chem. Phys.* **2007**, *126*, 026101. [[CrossRef](#)]
51. Kumari, R.; Kumar, R.; Open Source Drug Discovery Consortium; Lynn, A. G-mmpbsa -A GROMACS tool for high-throughput MM-PBSA calculations. *J. Chem. Inf. Model.* **2014**, *54*, 1951–1962. [[CrossRef](#)]
52. Tian, Y.; Shen, S.; Gu, L.; Zhou, J.; Li, Y.; Zheng, X. Computer-aided design of glucoside brain-targeted molecules based on 4PYP. *J. Mol. Graph. Model.* **2021**, *103*, 107819. [[CrossRef](#)] [[PubMed](#)]

**Disclaimer/Publisher’s Note:** The statements, opinions and data contained in all publications are solely those of the individual author(s) and contributor(s) and not of MDPI and/or the editor(s). MDPI and/or the editor(s) disclaim responsibility for any injury to people or property resulting from any ideas, methods, instructions or products referred to in the content.